Amplitude morphology of GPS radio occultation data for sporadic-*E* layers

Wen-Hao Yeh,[1] Cheng-Yung Huang,[2] Tung-Yuan Hsiao,[3] Tsen-Chieh Chiu,[1] Chien-Hung Lin,[4] and Yuei-An Liou[5]

Received 28 April 2012; revised 8 October 2012; accepted 8 October 2012; published 7 November 2012.

[1] Using the Global Positioning System radio occultation (GPSRO) technique, the observation of the global ionosphere becomes possible. The irregularity in the ionospheric sporadic-*E* (*Es*) layer, which is probably caused by wind shear, can be investigated by analyzing the signal-to-noise ratio (SNR) of RO signal. In this study, the relation between the amplitude of RO signals and the electron density profiles of the ionosphere is simulated, and RO data recorded in the time period from mid-2008 to mid-2011 are used for the analysis. Based on the simulation results, the multiple-layer-type (MLT) and the single-layer-type (SLT) *Es* layers which are defined by the shape of SNR, are used to analyze the global distribution of *Es* layer. The seasonal MLT *Es* layer is compared with the seasonal wind shear, which is obtained from the Horizontal Wind Model (HWM07). Furthermore, the seasonal MLT *Es* layer is compared with the SLT *Es* layer, and the global altitude distributions of MLT and SLT *Es* layers are similar while the magnitude distributions are different. Unlike the MLT *Es* layer, the global distribution of the SLT *Es* layer is similar to the distribution of *E* region peak electron density (N_mE), which is related to the solar zenith angle.

Citation: Yeh, W.-H., C.-Y. Huang, T.-Y. Hsiao, T.-C. Chiu, C.-H. Lin, and Y.-A. Liou (2012), Amplitude morphology of GPS radio occultation data for sporadic-*E* layers, *J. Geophys. Res.*, *117*, A11304, doi:10.1029/2012JA017875.

1. Introduction

[2] The Earth's ionosphere is an envelope containing partially ionized gas from about 60 to a thousand kilometers in altitude. The ionospheric *E* region ranges between 90 and 150 km. In the lower *E* region, a thin layer of enhanced electron density, called sporadic-*E* (*Es*) layer, appears sporadically in the altitude range from 90 to 120 km. The *Es* layer has been the subject of much research for many decades [e.g., *Whitehead*, 1970; *Whitehead*, 1989; *Mathews*, 1998] with the wind shear theory being the most likely explanation for the formation of this layer [*Whitehead*, 1961]. *Carrasco et al.* [2007] simulated the effect of winds and electric fields on the formation of the *Es* layer. Vertical shear in the zonal wind is an orientation requirement to establish the *Es* layer [*Kelley*, 2009]. *Pan and Tsunoda* [1999] and *Urbina et al.* [2000] observed quasiperiodic structures with descending echoing layers at altitudes above 100 km. *Pan and Tsunoda* [1999] also used semidiurnal neutral-wind variations to explain the slop sign reversals in the VHF radar observations. Furthermore, the seasonal dependence of the midlatitude *Es* layer is associated with the annual variation of meteor deposition [*Haldoupis et al.*, 2007].

[3] With the advent of Global Positioning System (GPS) technology, the global *Es* layer can be observed by using the radio occultation (RO) technique, which utilizes satellites at low Earth orbit (LEO) to receive GPS signals propagating through the atmosphere and ionosphere. *Hocke et al.* [2001] used data from the GPS/Meteorology experiment (GPS/MET) to find irregularities in the *Es* layer that occur at altitudes of 90–110 km. *Wu et al.* [2005] used German Challenging Minisatellite Payload (CHAMP) data to establish seasonal maps of the *Es* layer. In 2006, six LEO satellites were launched for the FORMosa SATellite Mission −3/ Constellation Observing System for Meteorology, Ionosphere, and Climate (FORMOSAT-3/COSMIC, or F-3). This system provides 2000–2500 profiles of high spatial and temporal resolutions for global analysis per day. *Arras et al.* [2008] used data from CHAMP, Gravity Recovery and Climate Experiment (GRACE), and F-3 to show the influence of the Earth's magnetic field on the *Es* layer. Furthermore, *Arras et al.* [2009] made a comparison between the occurrence of the *Es* layer and wind shear at midlatitudes based on the CHAMP, GRACE, and F-3 data.

[1]Department of Electrical Engineering, National Central University, Chung-Li, Taiwan.
[2]GPS Science and Application Research Center, National Central University, Chung-Li, Taiwan.
[3]Department of Information Technology, Hsing Wu Institute of Technology, New Taipei City, Taiwan.
[4]Department of Earth Science, National Cheng Kung University, Tainan, Taiwan.
[5]Center for Space and Remote Sensing Research, National Central University, Johng-Li, Taiwan.

Corresponding author: C.-Y. Huang, GPS Science and Application Research Center, National Central University, 300 Chung-Da Rd., Chung-Li 32001, Taiwan. (yusn2845@gmail.com)

0148-0227/12/2012JA017875

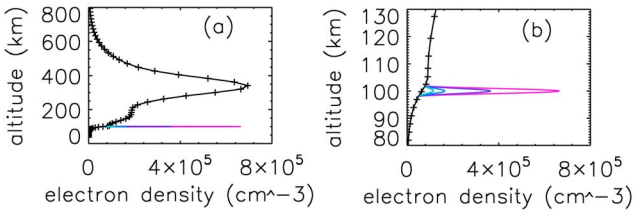

Figure 1. Electron density profiles for simulations. The black profile is the background electron density. The light blue, dark blue, purple, and pink profiles are the maximum electron density of *Es* layer added on the background electron density which are 0×10^5, 0.5×10^5, 1×10^5, 3×10^5, 6×10^5 cm^{-3}, respectively.

[4] In previous studies of the *Es* layer by using RO data, the relation between the *Es* layer electron density and its signature in the RO amplitude profile has been examined [e.g., *Wickert et al.*, 2004; *Pavelyev et al.*, 2007; *Yakovlev et al.*, 2008; *Yakovlev et al.*, 2010; *Zeng and Sokolovskiy*, 2010]. Nevertheless, the statistical analysis with the shape of RO amplitude has not yet received the proper attention. In this study, RO data recorded in the time period from mid-2008 to mid-2011 are used to derive the irregular degree (ID) from the RO signal-to-noise ratio (SNR) data to determine the altitude range and degree of the *Es* layer irregularities. Furthermore, the *Es* layer profiles are separated into the multiple layer type (MLT) and single layer type (SLT) by considering the shape of the SNR profile. The altitude distributions of the MLT and SLT *Es* layers are similar but the magnitude distributions are not. Besides the temporal and spatial analysis of the *Es* layer, the wind shear information as given by the Horizontal Wind Model (HWM07) [*Drob et al.*, 2008] is also used for comparison with the distribution of *Es* layer to examine the correlation between Es layer and wind shear. In Section 2, the RO amplitude profiles affected by SLT and MLT *Es* layers are simulated. In Section 3, the definition of the ID and the separation method of SLT and MLT RO amplitude profiles are described. A comparison of the results and a discussion are displayed and described in section 4, followed by summary.

2. Relation Between Electron Density and Amplitude Profiles

[5] In this study, the *Es* layer profiles are separated into the MLT and SLT. In order to differentiate between these two types of *Es* layers, a ray tracing algorithm is used to retrieve the amplitude profiles from the prescribed electron density profiles. The electron density profiles used for the simulations are shown in Figure 1. The black plus signed line is the background electron density profile obtained from the Thermosphere Ionosphere Electrodynamics General Circulation Model (TIEGCM) result. The light blue, dark blue, purple, and pink lines are the profiles of *Es* layers. The altitude, thickness and horizontal extension of *Es* layer are 90–110 km, 0.5–5 km and 10–1000 km, respectively [*Wu et al.*, 2005]. In this study, the altitude, maximum thickness, and horizontal extension of *Es* layer are set to be 100 km, 4 km and 500 km, respectively. The electron density distribution $N_e(x, y)$ is given by:

$$
\begin{aligned}
&N_e(x,y) = N_b + N_{Es}(x,y)\\
&N_{Es}(x,y) = P(x) + N_{\max}\cos\left[\frac{(x-x_0)\pi}{500}\right]\cos\left\{\frac{(y-y_0)\pi}{4\cos\left[\frac{(x-x_0)\pi}{500}\right]}\right\},\\
&\quad if\ -\frac{\pi}{2} < \frac{(x-x_0)\pi}{500} < \frac{\pi}{2}\ and\ -\frac{\pi}{2} < \frac{(y-y_0)\pi}{4\cos\left[\frac{(x-x_0)\pi}{500}\right]} < \frac{\pi}{2}\\
&P(x) = \sum_1^n A_n \sin\left(2\pi(x-x_0)\frac{W_n}{500}\right)\\
&N_{Es}(x,y) = 0, else
\end{aligned}
\tag{1}
$$

where, N_b, N_{Es}, $N_{\max}$, P, and (x_0, y_0) are the background electron density, electron density of *Es* layer, the maximum electron density of *Es* layer, the perturbation function, and the coordinate of the maximum electron density of *Es* layer, respectively. The background electron density profile (N_b) in Figure 1 is result of TIEGCM model. The perturbation function is formed by several sine waves with different amplitudes (A_n) and wave numbers (W_n). One of the N_{Es}, considering the curvature to conform the 100 km in altitude and $P(x)$ is set to be 0, used for simulation is shown in Figure 2 (top). The *Es* layer is often affected by the external forces and irregularities can take place. The effect of gravity waves on the N_{Es} is investigated by introducing gravity-wave-related perturbation. Two different cases of perturbation are examined, and the Earth's curvature is also considered (cf. Figure 2). In Figure 2, the center of the Earth is located at (0,0), (x_0, y_0) is set to be (0,6480.744), and the radius of the Earth is set to be 6380.744 km. In Figure 2 (middle), n is set to be 3, and A_1, A_2,

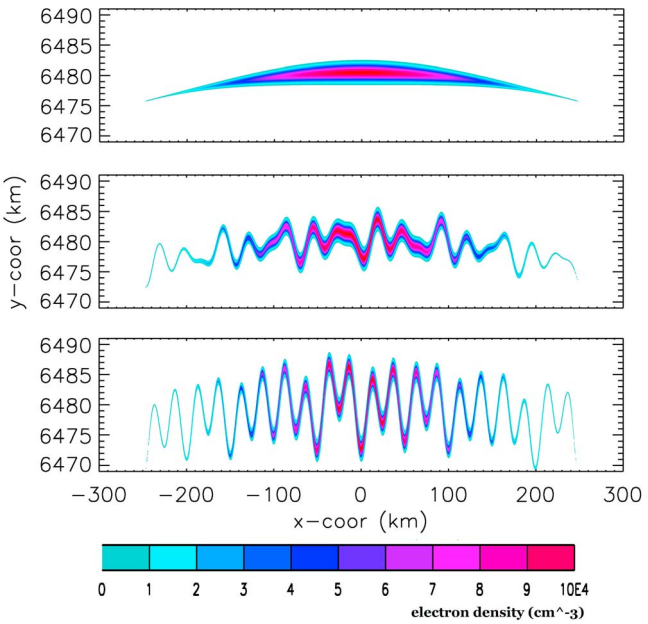

Figure 2. Horizontal distribution of *Es* layers which have (top) no irregularity and (middle and bottom) have irregularities.

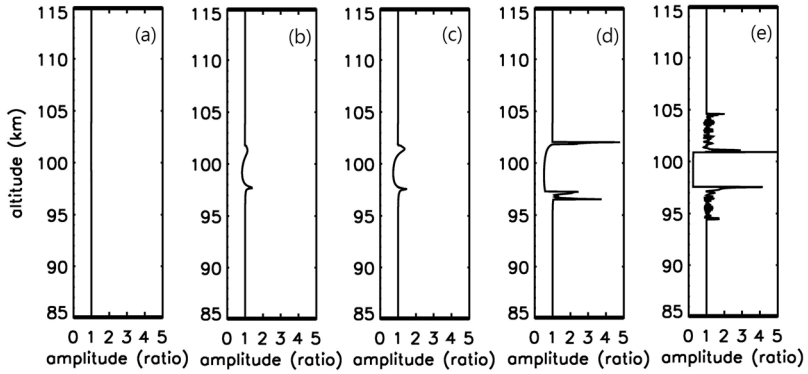

Figure 3. Simulated amplitude profiles by using the background electron density profile and different added electron density of *Es* layer. The shape of the added *Es* layer is like the shape in Figure 2 (top) which has no irregularity. The maximum electron density of *Es* layer added on the background electron density from Figure 3a to Figure 3e are 0×10^5, 0.5×10^5, 1×10^5, 3×10^5, 6×10^5 cm^{-3}, respectively.

A_3, W_1, W_2, and W_3 are set to be 1.2, 1.8, 1, 20, 14, and 8, respectively. In Figure 2 (bottom), n is set to be 4, and A_1, A_2, A_3, A_4, W_1, W_2, W_3, and W_4 are set to be 1.2, 1.8, 1, 5, 6, 10, 8, and 20, respectively. In the simulations, the *Es* layer is located at the tangent point of signal trajectories, and the frequency of the signal is 1.575 GHz (L1). The ray tracing algorithm in W.-H. Yeh et al. (Ray tracing simulation in nonspherically symmetric atmosphere for GPS radio occultation, submitted to *GPS Solutions*, 2012) is used to integrate signal trajectory. The energy flux calculation method in *Sokolovskiy* [2000] is used to estimate amplitude profiles.

[6] The simulations for the profiles of the RO signal amplitude with different maximum electron density of *Es* layer are shown in Figures 3 and 4. The shape of *Es* layer in Figure 2 (top) is used to simulate the amplitude profiles in Figure 3. The simulation results by using $N_{max} = 0 \times 10^5$, 0.5×10^5, 1×10^5, 3×10^5, and 6×10^5 are shown in Figures 3a–3e, respectively. In the ionosphere, the refractive index decreases as the electron density increases [*Davies*, 1990]. The signal propagating in the ionosphere is bent due to the refractivity gradient. The bent signal trajectory causes a focusing/debunching phenomenon in the amplitude profile. In Figure 3a, the amplitude of signal has no obvious shake, which indicates that the effect of the background profile is very little. The positive/negative humps in Figures 3b and 3c, which are the local maximum/minimum in the profiles, are due to the focusing/debunching of the signal propagating through the *Es* layer. According to the geometrical optics, focusing/debunching of signal occurs if $d^2 Ne/dh^2$ is positive/negative, where Ne and h are electron density and altitude, respectively. When the electron density of *Es* layer is large, the interference phenomenon will occur in the focusing parts of amplitude profile, and shown in Figures 3d and 3e. The simulation results of the shape of *Es* layer in the first and second panels of Figure 2 are shown in Figures 4a and 4b, respectively. Due to the irregularity of *Es* layer, the refractivity gradient in the signal trajectories is more complex and cause irregular perturbation in amplitude profiles. The irregularity of the *Es* layer in the third panel of Figure 2 is larger than in the second panel. The larger irregularity of *Es* layer often causes the larger irregular degree of irregular amplitude.

[7] Comparing the electron density with the simulated amplitude profiles in Figures 2–4, it is found that the distribution of amplitudes in Figures 3b–3e show an obvious characteristic. Due to the relation between the electron density and amplitude profiles, the distribution of amplitude has one negative hump and its altitude is very close to the altitude of the dense layer of electron density profiles. There are two positive humps (type-I) or two interference portions (type-II) located at the top and bottom of the electron density layer. Four examples of observational amplitude profiles are shown in Figures 5a–5d (left). Figures 5a–5b (left) are type-I and type-II SLT amplitude profiles, respectively. Figure 5c (left) is MLT amplitude profile. The shape characteristics of the

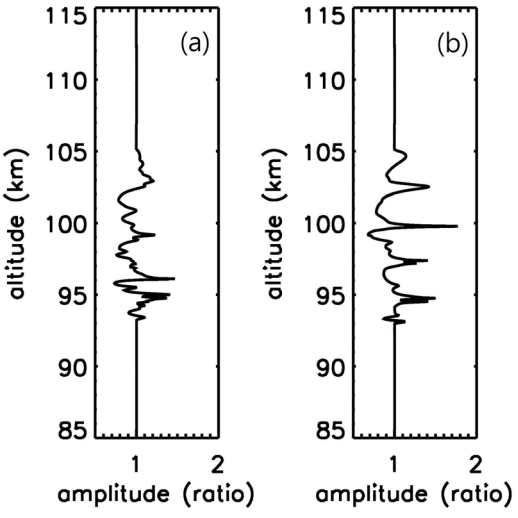

Figure 4. Simulated amplitude profiles by using the background electron density profile and different shape of added *Es* layer. The shape and electron density distribution of added *Es* layer used for Figure 4a and Figure 4b are in the middle and lower panels in Figure 3, respectively.

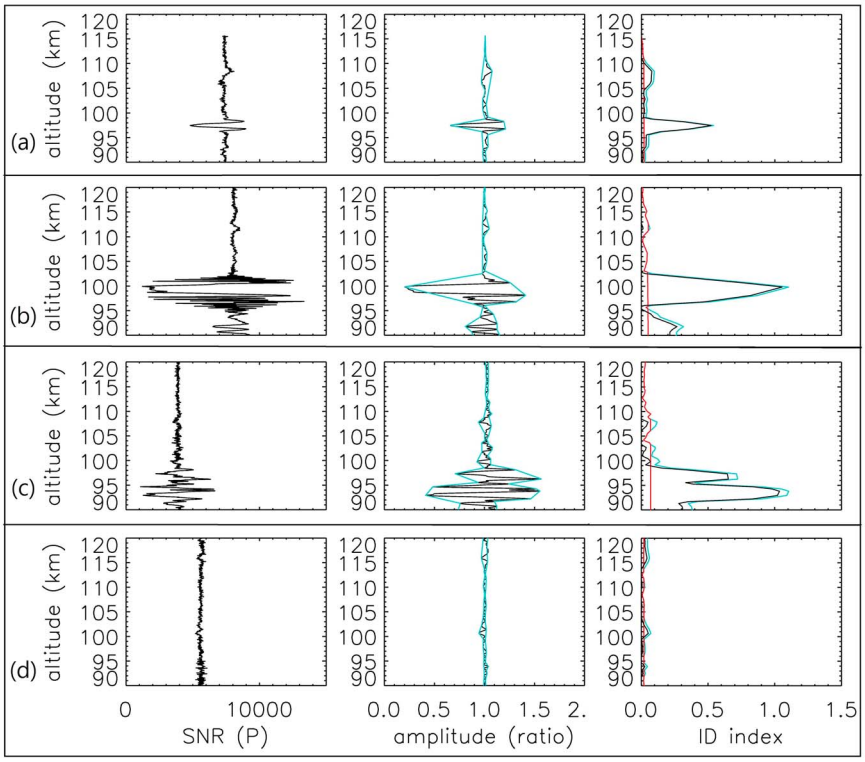

Figure 5. Profiles of SNR, ID index, and intermediate productions (amplitude ratio) of three different type fluctuations: (a) type-I SLT (atmPhs_C004.2010.036.00.30.G07_2010.2640_nc), (b) type-II SLT (atmPhs_C005.2009.244.21.44.G10_2010.2640_nc), (c) MLT (atmPhs_C001.2010.029.01.35.G14_2010.2640_nc), and (d) noisy type (atmPhs_C005.2010.072.00.28.G28_2010.2640_nc).

amplitude profiles in these panels conform to the simulated results. Figure 5d (left) shows that the amplitude profile is not affected by the *Es* layer.

3. Analysis Method

[8] Compare with the simulation and observation results, the large perturbation of amplitude in observation data is caused by ionospheric irregularities. In order to study the irregularities, the ID index is defined and calculated in the following three steps:

[9] (1) Change the SNR to the relative amplitude. The average upper altitude of the high rate (50 Hz) GPS occultation measurement of F-3 is 120 km [*Wickert et al.*, 2009]. Generally, the value of SNR begins to decrease due to the effect of the neutral atmosphere below 40 km in altitude. Therefore, the analysis in this study is conducted from 50 to 120 km in altitude. The average value of SNR from 50 to 120 km is the normalizing factor. The relative amplitude is obtained by dividing SNR with the normalizing factor.

[10] (2) Smooth the relative amplitude profile. The smooth process is used to remove the noise in relative amplitude profiles. The smooth method $f_s = [I + S^T \Gamma S]^{-1} f_u$ [*Feng and Herman*, 1999], where f_s, f_u, I, S, and Γ are the smoothed result, raw data, unitary matrix, constraint smoothing matrix, and diagonal matrix with degrees control element, respectively, is used in this study. The normalized and smoothed relative amplitude profiles are the black lines shown in Figures 5a–5d (middle).

[11] (3) Decompose the amplitude into upper and lower envelopes by using empirical mode decomposition (EMD) [*Huang et al.*, 1998]. It should be noted that in order to avoid distorting the analysis results, the linear connection is replaced with a cubic spline to connect the local maxima/minima for the upper/lower envelopes. The upper and lower envelopes are the blue lines shown in Figures 5a–5d (middle).

[12] (4) Derive pre-ID index by using the value of the upper envelope minus that of the lower envelope. The pre-ID index profiles are the blue lines shown in Figures 5a–5d (right).

[13] (5) Derive ID index profile by using the value of pre-ID index profile without the background profile. In the unaffected portion of the *Es* layer, the background profile is the pre-ID index profile. In the affected portion of the *Es* layer, the background profile is set to be a linear portion between the unaffected upper and lower portions. The background and ID index profiles are represented by the red and black lines shown in Figures 5a–5d (right), respectively.

[14] Comparing the SNR and ID profiles in Figure 5, it is found that the altitude range and the large ID index correspond to that of the large irregularity in the SNR profiles.

[15] The high rate (50 Hz) of L1 GPS occultation SNR data of F-3 recorded from the 181st day of 2008 to the 180th day of 2011 are used for data analysis. We divided the year into four seasons (based on the northern hemisphere): winter is from December to February, spring is from March to May, summer is from June to August, and autumn is from September to November. All data except the SLT data

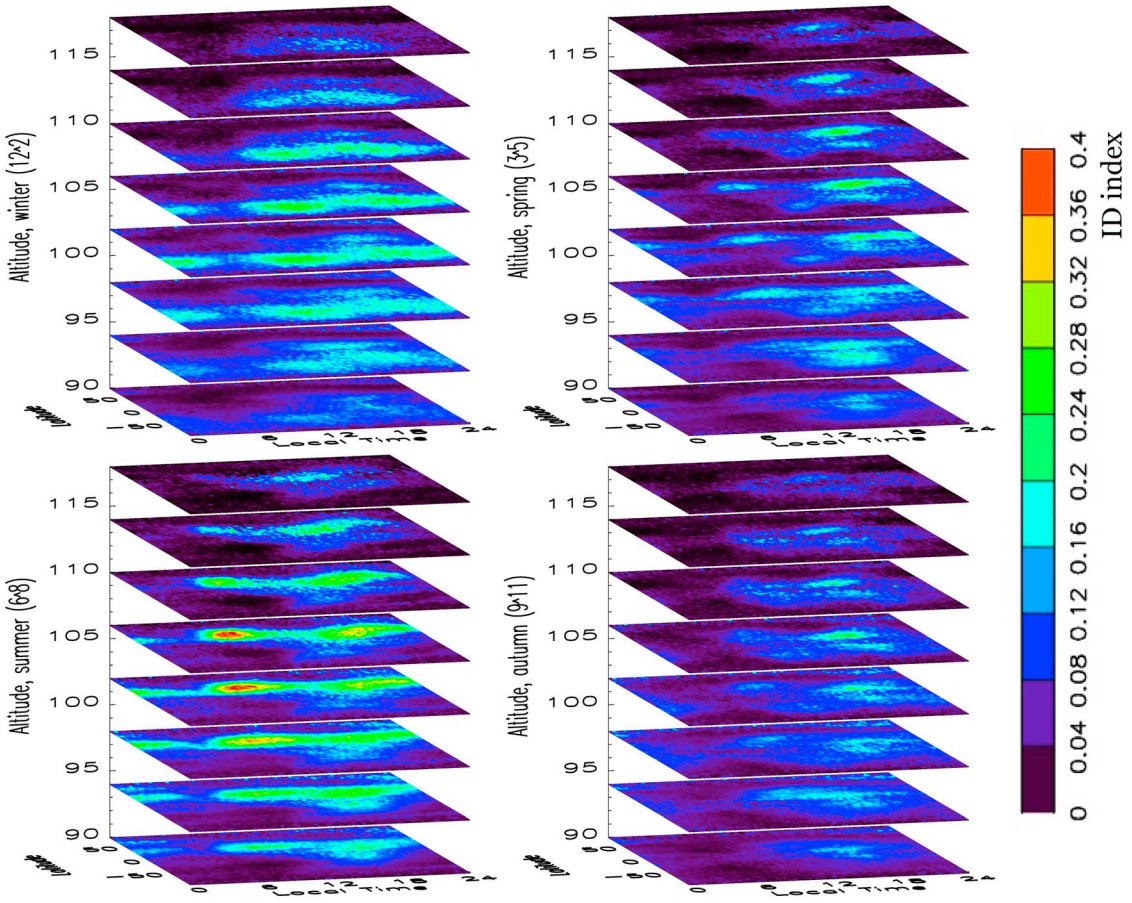

Figure 6. Local time-latitude-altitude analysis of the ID index of the MLT *Es* layer in four seasons.

are used for the 3-dimensional local time-geographic latitude-altitude (LT-Lat-Alt) analysis. We average the individual ID index value over 20 min in local time, 5° in geomagnetic latitude, and 1 km in altitude, while the coordinates of the center are shifted every 4 min and 1° along local time and geomagnetic latitude, respectively.

[16] In addition to data analysis, the SLT data is separated from all RO data. The SNR profile is regarded as type-I SLT profile if it satisfies following conditions: (i) The altitude of the maximum ID (maxID) corresponds to a negative hump; (ii) At the upper and lower altitude of maxID, there are two positive humps near the negative hump at the altitude of maxID. Two ID values correspond to these two positive humps are denoted as ID_S and ID_L. The value of ID_L is larger than ID_s. In this condition, ID_S/ID_L should larger than 2/3; (iii) the nearest negative hump at each upper and lower altitudes of the maxID is smaller than one third of maxID; (iv) except the altitude region of (iii), the ID of the SNR profile is not larger than one third of the maxID. The SNR profile is regarded as type-II SLT profile if it satisfies following conditions: (i) The SNR profile satisfies the *Es* event identified conditions in *Zeng and Sokolovskiy* [2010]; (ii) The standard deviation profile of relative amplitude calculated in 1 km interval has only two local maximum which are larger than 0.2. The value 0.2 is an empirically found threshold to separate the general amplitude and interference amplitude. And the two local maximum indicate two interference portions located at the top and bottom of the electron density layer. The ratio of the SLT and all data is about 1:50. Due to the small amount of SLT data, it cannot be used for LT-Lat-Alt analysis. The local time-latitude (LT-Lat) distribution of maxID and altitude of SLT data are used for analysis. We average the individual ID index value over 28 min in local time, 7° in geomagnetic latitude, while the coordinates of the center are shifted every 4 min and 1° along local time and geomagnetic latitude, respectively.

4. Analysis Results and Discussions

4.1. MLT *Es* Layer Distribution

[17] The 3-dimensional LT-Lat-Alt analysis of all data except for the SLT data for the four seasons is shown in Figure 6. This can be regarded as the analysis of the MLT *Es* layer with 510–570 thousand pieces of data used for analysis for each season. The maximum value of ID index is identified at about 100–108 km in altitude. In summer, in the northern hemisphere, there is a clear semidiurnal pattern of high ID with two ribbons, the morning ribbon (MR) and the afternoon ribbon (AR) that occurs from 90 to 120 km in altitude, which is the range in which the *Es* layer appears [*Arras et al.*, 2008]. The maximum of MR and AR occur around 10:00 and 20:00LT, which agree with *Wu et al.* [2005]. In winter, there is a clear semidiurnal pattern, which is similar to the pattern in summer, also occurs in the southern hemisphere while the maximum

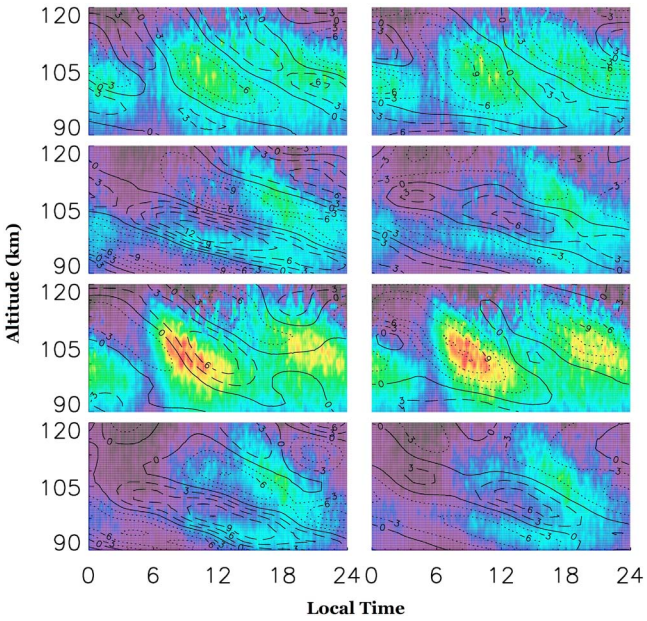

Figure 7. Distribution of the ID index of the MLT *Es* layer and wind shear. The seasons and latitudes in the figure are winter at −40°, spring at 20°, summer at 40°, and autumn at 20° (top to bottom). Color code is similar to Figure 3, which are ID index distributions of the MLT *Es* layer. Contour (left) meridional and (right) zonal wind shear. The zero, negative and positive wind shear are marked by solid, dotted and dashed isolines, respectively, for meridional and zonal wind shear.

MR occurs about one hour later than in summer. In winter/summer, a diurnal pattern occurs in the northern/southern hemisphere with a maximum around 1500LT. The latitude of where patterns occur in southern/northern in winter/summer is about −40°/40°, and in northern/southern in winter/summer is about 15°/−5°, which are agree with *Arras et al.* [2009]. In the northern hemisphere in spring and autumn, the maximum of MR and AR occurrence time is similar to the occurrence time in the southern hemisphere in winter, while in the southern hemisphere the MR and AR occurrence times are closer to noon, about 11:00LT and 17:00LT, respectively. The latitude of where patterns occur in spring/autumn in the northern and southern hemisphere are about 20° and −20°, respectively, which agree with *Arras et al.* [2009]. A comparison of the ID magnitudes in the four seasons shows that the summer maximums agree with *Haldoupis et al.* [2007] and *Arras et al.* [2009].

4.2. Comparison Between Horizontal Wind Shear and MLT *Es* Layer

[18] *Arras et al.* [2009] studied the occurrence frequency of the *Es* layer from 80 to 100 km by using the wind shear information from the Collm Observatory. In this study, HWM07, which is a statistical representation of the horizontal wind fields of the Earth's atmosphere from the ground to the exosphere (0–500 km) [*Drob et al.*, 2008], is used to calculate the wind shear in the *Es* layer region. The distribution of the wind shear in 2010 and ID index distribution for all four seasons are shown in Figure 7. In the figure, the distributions are shown at latitudes of −40, 20, 20, and 40, which are near the latitude where the maximum ID index occurs, in winter, spring, summer and autumn, respectively. The contours in Figure 7 show the mean wind shear from 90 to 120 km in altitude in 2010 for the four seasons as obtained by using HWM07. The zero, negative and positive wind shears are marked by solid, dotted and dashed isolines, respectively, in the meridional and zonal wind shear panels in Figure 7. The color codes indicate the ID index distributions of the MLT *Es* layer. Negative wind shear is required for *Es* layer formation [*Arras et al.*, 2009]. The ID index distributions agree with the negative zonal wind shear for winter and summer, and the negative meridional wind shear for winter. Nevertheless, the agreement with wind shear is not obvious in spring and autumn although the large ID index also distributes in the negative meridional or zonal wind region. The global zonal wind shear distributions at the corresponding altitude of the maxID of the MLT *Es* layer in the four seasons are shown in Figure 8 (right). It is found that in the maxID distributions of the MLT *Es* layer, which are shown in Figure 8 (middle), the high maxID index is related to the high negative zonal wind shear, especially in summer. Compare the middle and right panels of Figure 8 with Figure 7, the distribution of MLT *Es* layer is correlated with the negative wind shear.

4.3. SLT *Es* Layer Distribution

[19] The LT-Lat analyses of maxID and its corresponding altitude of the SLT and MLT *Es* layers are shown in Figures 8 and 9. Due to the lack of the SLT data at high latitudes, we only show the results in latitude ranges from −70° to 70°. The maxID distributions for the four seasons are shown in Figure 8. The semidiurnal and diurnal of the MLT *Es* layer have been described above. Unlike those in the MLT layer, the maxID distributions of the SLT *Es* layer in the four seasons are very similar to one another. Furthermore, the maxID distributions of the SLT *Es* layer are also similar to the distribution of the *E* region peak electron density (N_mE) [e.g., *Nicolls et al.*, 2012], which begins to increase at dawn, reaches its maximum at noon, and then decreases until dusk. The maxID's altitude distributions in the four seasons are shown in Figure 9. It is found that altitude distributions of the SLT and MLT *Es* layers in each season are similar to one another, and are different from the distribution of the altitude of the *E* region peak (h_mE) [e.g., *Nicolls et al.*, 2012].

[20] Based on the similar altitude distributions of the SLT and MLT *Es* layers in Figure 9, it is found that the SLT *Es* layer is almost coexist with the MLT *Es* layer. However, their different maxID distributions indicate that their formation mechanisms are different. From the comparison described in the last subsection and former studies [e.g., *Arras et al.*, 2009], the MLT *Es* layer is probably formed by wind shear, and the SLT *Es* layer, whose maxID distributions in the four seasons are like the distribution of N_mE, is associated with the solar zenith angle. The *Es* layer is formed in the region where the vertical electron velocity is zero and the gradient of vertical velocity is large [*Whitehead*, 1961]. During and after the formation of the *Es* layer, some irregular structures are caused by the effect of certain external forces, such as the wind shear and gravity waves. The irregular structures in

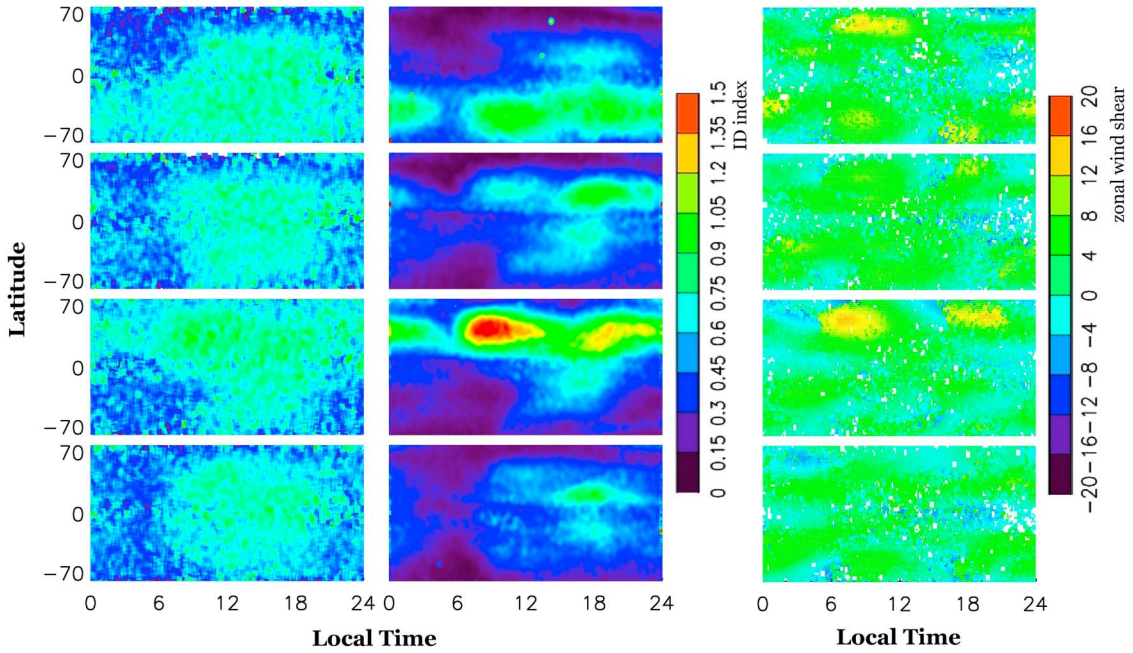

Figure 8. Distributions of maximum irregular degree (maxID) of the (left) SLT and (middle) MLT *Es* layers in four seasons (top to bottom: winter, spring, summer, and autumn). In order to compare two of them more easily, the ID index of the MLT *Es* layer has been multiplied by four. (right) The zonal wind shear distribution at the corresponding altitude of maxID of the MLT *Es* layer in four seasons, which are shown in Figure 6 (right).

the *Es* layer have been observed and simulated in former studies [e.g., *Miller and Smith*, 1978; *Huang and Kelley*, 1996; *Cosgrove and Tsunoda*, 2003]. In contrast to the simulations in this study and the above description, the MLT *Es* layer is caused by irregular structures. Otherwise, the SLT *Es* layer can be regarded as an *Es* layer which has not been influenced by external forces. In the simulations, the amplitude profiles of the SLT *Es* layer are purer than the MLT *Es* layer with only one negative hump with two positive humps or two interference portions on either side. Although the amplitude profile is associated with the vertical gradient of the electron density, the maxID of the SLT *Es* layer can also be indicated by the magnitude of the electron density in the layer. With the smaller solar zenith angle, the ionization rate becomes larger in the *E* region. With a larger electron density in *E* region, a higher electron density is formed in the *Es* layer. Therefore it is reasonable that the maxID distributions of the SLT Es layer are similar to the N_mE distribution. Furthermore, from the above description, the difference between the wind shear and MLT *Es* layer distributions in four seasons shown in Figure 7 can be further explained. In winter and summer, the large irregularities of MLT *Es* layer occur in the large wind shear regions, while it is not the case, although the irregularities still occur in the negative wind shear regions in spring and autumn. In winter and summer, the large wind shear regions contain the regions of *Es* layer and cause the large irregularities in the regions. In spring and autumn, the large negative wind shear regions do not cover the regions of *Es* layer formation, while the small negative wind shear regions do cover the regions of *Es* layer. So, in spring and autumn, the irregularities only occur in the small wind shear regions.

5. Summary

[21] In this study, we have simulated the amplitude profiles of four electron density profiles to confirm the relation

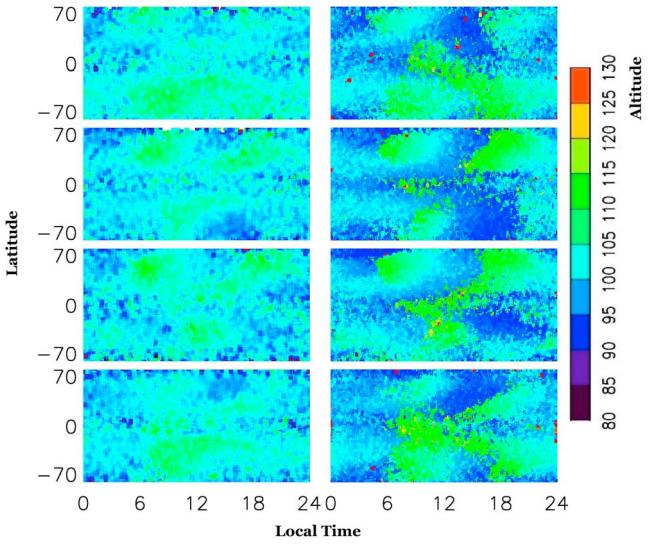

Figure 9. Distributions of altitude of the (left) SLT and (right) MLT *Es* layers in four seasons (top to bottom: winter, spring, summer, and autumn).

between the amplitude and the electron density. Based on the simulation results, it is found that the MLT and SLT *Es* layers can be separated by considering the shape of SNR profiles. A large amount of the F-3 SNR data recorded in three years has been used for the analysis in which the ID index is defined. The distributions of the MLT *Es* layer in the four seasons are in agreement with those obtained in previous studies. The wind shear information obtained from HWM07 in four seasons in 2010 is compared with the global distribution for the MLT *Es* layer. Furthermore, the comparison of the MLT and SLT *Es* layers shows that the maxID distributions of both layers are different while the distributions of the maxID altitude are similar. Unlike the MLT *Es* layer, which is probably formed by wind shear, the SLT *Es* layer is mainly associated with the solar zenith angle.

[22] **Acknowledgments.** The authors would like to thank the support from National Space Organization (NSPO), GPS Science and Application Research Center. The research is supported by grant NSC-100-2119-M-008-011 and NSC-100-2119-M-006-013.

[23] Robert Lysak thanks the reviewers for their assistance in evaluating this paper.

References

Arras, C., J. Wickert, G. Beyerle, S. Heise, T. Schmidt, and C. Jacobi (2008), A global climatology of ionospheric irregularities derived from GPS radio occultation, *Geophys. Res. Lett.*, *35*, L14809, doi:10.1029/2008GL034158.

Arras, C., C. Jacobi, and J. Wickert (2009), Semidiurnal tidal signature in sporadic *E* occurrence rates derived from GPS radio occultation measurements at higher midlatitudes, *Ann. Geophys.*, *27*, 2555–2563, doi:10.5194/angeo-27-2555-2009.

Carrasco, A. J., I. S. Batista, and M. A. Abdu (2007), Simulation of the sporadic *E* layer response to prereversal associated evening vertical electric field enhancement near dip equator, *J. Geophys. Res.*, *112*, A06324, doi:10.1029/2006JA012143.

Cosgrove, R. B., and R. T. Tsunoda (2003), Simulation of the nonlinear evolution of the sporadic-*E* layer instability in the nighttime midlatitude ionosphere, *J. Geophys. Res.*, *108*(A7), 1283, doi:10.1029/2002JA009728.

Davies, K. (1990), *Ionospheric Radio*, Peter Peregrinus, London, doi:10.1049/PBEW031E.

Drob, D. P., et al. (2008), An empirical model of the Earth's horizontal wind fields: HWM07, *J. Geophys. Res.*, *113*, A12304, doi:10.1029/2008JA013668.

Feng, D. D., and B. M. Herman (1999), Remotely sensing the Earth's atmosphere using the Global Positioning System (GPS)—The GPS/MET data analysis, *J. Atmos. Oceanic Technol.*, *16*, 989–1002, doi:10.1175/1520-0426(1999)016<0989:RSTESA>2.0.CO;2.

Haldoupis, C., D. Pancheva, W. Singer, C. Meek, and J. MacDougall (2007), An explanation for the seasonal dependence of midlatitude sporadic *E* layer, *J. Geophys. Res.*, *112*, A06315, doi:10.1029/2007JA012322.

Hocke, K., K. Igarashi, M. Nakamura, P. Wilkinson, J. Wu, A. Pavelyev, and J. Wikert (2001), Global sounding of sporadic *E* layers by the GPS/MET radio occultation experiment, *J. Atmos. Sol. Terr. Phys.*, *63*, 1973–1980, doi:10.1016/S1364-6826(01)00063-3.

Huang, C.-S., and M. C. Kelley (1996), Numerical simulations of gravity wave modulation of midlatitude sporadic *E* layers, *J. Geophys. Res.*, *101*(A11), 24,533–24,543, doi:10.1029/96JA02327.

Huang, N. E., Z. Shen, S. R. Long, M. C. Wu, H. H. Shin, Q. Zheng, N.-C. Yen, C. C. Tung, and H. H. Liu (1998), The empirical mode decomposition and the Hilbert spectrum for nonlinear and non-stationary time series analysis, *Proc. R. Soc. London, Ser. A*, *454*, 903–995, doi:10.1098/rspa.1998.0193.

Kelley, M. C. (2009), *The Earth's Ionosphere: Plasma Physics and Electrodynamics*, 2nd ed., Academic, San Diego, Calif.

Mathews, J. D. (1998), Sporadic *E*: Current views and recent progress, *J. Atmos. Sol. Terr. Phys.*, *60*(4), 413–435, doi:10.1016/S1364-6826(97)00043-6.

Miller, K. L., and L. G. Smith (1978), Incoherent scatter radar observations of irregular structure in mid-latitude sporadic *E* layers, *J. Geophys. Res.*, *83*(A8), 3761–3775, doi:10.1029/JA083iA08p03761.

Nicolls, M. J., F. S. Rodrigues, and G. S. Bust (2012), Global observations of *E* region plasma density morphology and variability, *J. Geophys. Res.*, *117*, A01305, doi:10.1029/2011JA017069.

Pan, J. C., and R. T. Tsunoda (1999), Semidiurnal behavior of quasi-period echoes in the mid-latitude Es region observed with the Chung-Li VHF radar, *Geophys. Res. Lett.*, *26*, 2621–2624, doi:10.1029/1999GL900562.

Pavelyev, A. G., Y. A. Liou, J. Wickert, T. Schmidt, A. A. Pavelyev, and S. F. Liu (2007), Effects of the ionosphere and solar activity on radio occultation signals: Application to CHAllenging Minisatellite Payload satellite observations, *J. Geophys. Res.*, *112*, A06326, doi:10.1029/2006JA011625.

Sokolovskiy, S. V. (2000), Inversions of radio occultation amplitude data, *Radio Sci.*, *35*, 97–105, doi:10.1029/1999RS002203.

Urbina, J., E. Kudeki, S. J. Franke, S. Gonzalez, Q. Zhou, and S. C. Collins (2000), 50 MHz radar observations of mid-latitude *E*-region irregularities at Camp Santiago, Puerto Rico, *Geophys. Res. Lett.*, *27*, 2853–2856, doi:10.1029/2000GL000028.

Whitehead, J. D. (1961), The formation of the sporadic-*E* layer in the temperate zones, *J. Atmos. Terr. Phys.*, *20*, 49–58, doi:10.1016/0021-9169(61)90097-6.

Whitehead, J. D. (1970), Production and prediction of sporadic *E*, *Rev. Geophys.*, *8*, 65–144, doi:10.1029/RG008i001p00065.

Whitehead, J. D. (1989), Recent work on mid-latitude and equatorial sporadic-*E*, *J. Atmos. Terr. Phys.*, *51*(5), 401–424, doi:10.1016/0021-9169(89)90122-0.

Wickert, J., A. G. Pavelyev, Y. A. Liou, T. Schmidt, C. Reigber, K. Igarashi, A. A. Pavelyev, and S. Matyugov (2004), Amplitude variations in GPS signals as possible indicator of ionospheric structures, *Geophys. Res. Lett.*, *31*, L24801, doi:10.1029/2004GL020607.

Wickert, J., et al. (2009), GPS radio occultation: Results from CHAMP, GRACE and FORMOSAT-3/COSMIC, *Terr. Atmos. Oceanic Sci.*, *20*, 35–50, doi:10.3319/TAO.2007.12.26.01(F3C).

Wu, D. L., C. O. Ao, G. A. Hajj, M. de la Torre Juarez, and A. J. Mannucci (2005), Sporadic *E* morphology from GPS-CHAMP radio occultation, *J. Geophys. Res.*, *110*, A01306, doi:10.1029/2004JA010701.

Yakovlev, O. I., J. Wickert, A. G. Pavelyev, S. S. Matyugov, and V. A. Anufriev (2008), Sporadic structures in equatorial ionosphere as revealed from GPS occultation data, *Acta Astronaut.*, *63*, 1350–1359, doi:10.1016/j.actaastro.2008.05.023.

Yakovlev, O. I., J. Wickert, A. G. Pavelyev, V. A. Anufriev, and G. P. Cherkunova (2010), Results of radio occultation measurement of polar ionosphere at links satellite-to-satellite during strong flare solar activity, *Acta Astronaut.*, *67*, 315–323, doi:10.1016/j.actaastro.2010.02.017.

Zeng, Z., and S. Sokolovskiy (2010), Effect of sporadic *E* cloud on GPS radio occultation signal, *Geophys. Res. Lett.*, *37*, L18817, doi:10.1029/2010GL044561.